Toward Impedance Control in Human-Machine Interfaces for Upper-Limb Prostheses

Laura Ferrante, Mohan Sridharan, Claudio Zito, and Dario Farina, *Fellow, IEEE*

***Abstract*— *Objectives:* Adaptation of upper-limb impedance (stiffness, damping, inertia) is crucial for humans to physically interact with the external environment during grasping and manipulation tasks. We present a novel framework for Adaptive Impedance Control of Upper-limb Prosthesis (AIC-UP) based on surface electromyography (sEMG) signals. *Methods:* AIC-UP uses muscle-tendon models driven by sEMG signals from agonist-antagonist muscle groups to estimate human motor intent as joint kinematics, stiffness, and damping. These estimates are used to implement a variable impedance controller on a simulated robot. Designed for use by amputees, joint torque or stiffness measurements are not used for model calibration. AIC-UP was evaluated with eight able-bodied subjects and a transradial amputee performing target-reaching tasks in simulation through wrist flexion-extension. The control performance was tested in free space and in the presence of unexpected perturbations. *Results:* AIC-UP outperformed a neural network that regresses the desired kinematics from sEMG signals, in terms of robustness to muscle coactivations needed to complete the task. These results were in agreement with the qualitative feedback from participants. Additionally, AIC-UP enabled the user to adapt the stiffness and damping to the tasks at hand.**

***Index Terms*— Myocontrol, impedance control, human motor intent, muscle-skeleton models, prostheses.**

I. Introduction

HUMANS use coactivation of agonist-antagonist muscles to modulate the limb impedance in a time- and task-dependent manner, independently from the limb kinematics [1]. Estimation of the motor intent in terms of joint kinematics and impedance would therefore be relevant when substituting missing limbs with artificial ones. However, enabling a user to voluntarily control the impedance of even just a single Degree of Freedom (DoF) of an upper-limb prosthesis is still an open problem. Our work aims to enable variable impedance control of upper-limb prostheses; we describe a framework that comprises simplified muscle-tendon models to extract three degrees of control (kinematics, stiffness, and damping) for a single DoF using low-density surface electromyographic (sEMG) signals, in the absence of a reference joint torque and stiffness. Here we first review methods that use low-density sEMG signals to control a (simulated) prosthesis, including methods that estimate the motor intent only as kinematics (Section I-A), and those that also estimate and use the joint impedance parameters in the controllers (Section I-B). We then describe our contributions (Section I-C).

This work was supported in part by a studentship from the UK Engineering and Physical Sciences Research Council *Physical Sciences for Health* Centre for Doctoral Training (EP/L016346/1) and partially by the European Research Council Synergy Grant Natural BionicS (810346).

Laura Ferrante was with the School of Computer Science, University of Birmingham, Birmingham B15 2TT, U.K. She is now with the Bioengineering Department, Imperial College London, London W12 0BZ, U.K. (e-mail: l.ferrante@imperial.ac.uk). Mohan Sridharan is with the School of Informatics at the University of Edinburgh, Edinburgh EH8 9AB, U.K. (e-mail: m.sridharan@ed.ac.uk). Claudio Zito is with the School of Mathematical & Computer Sciences, Dubai, Heriot-Watt University Dubai, Dubai PO Box 38103, U.A.E. (e-mail: C.Zito@hw.ac.uk). Dario Farina is with the Bioengineering Department, Imperial College London, London W12 0BZ, U.K. (e-mail: d.farina@imperial.ac.uk).

A. Estimation of motor intent as kinematics

Many methods have been developed to learn a mapping from sEMG signals to target kinematics (i.e., joint kinematics or motion classes). These include pattern-recognition methods [2], [3], regression-based [4]–[6], and unsupervised ones [6]–[8]. In recent times, deep learning methods are increasingly being used to extract sEMG features and learn complex non-linear mapping between sEMG signals and target kinematics [4], [9]–[14]. However, the robustness of these methods has not been tested during control tasks that require substantial changes in the coactivation of muscles (i.e., limb impedance), making it unclear whether the control performance of the algorithms deteriorates in these tasks. In addition to data-driven approaches, progresses in musculoskeletal modelling have provided physiologically accurate kinematics and motion dynamics predictions. Muscle-tendon models (MTUs) are used to estimate muscle-tendon forces, and predict the body kinematics and dynamics of motion given the input sEMG signals. The complexity of such simulations, determined by the number of MTUs and the approach used to model MTUs, is a trade-off between physiological accuracy in the predictions [15]–[17] and computational cost [18]–[20]. This is crucial in applications that have real-time constraints, such as prosthesis control. Moreover, the inability to measure physiological parameters (e.g., moment arms) needed for model identification, makes complex MTUs-based simulations impractical when muscles may be (partly) missing. Lumped muscle-tendon models have been introduced to limit the modelling complexity by reducing the number of MTUs and thus the number of sEMG recordings sites [21]–[23]. In these methods, muscles with the same functionality (e.g., agonist muscles) are modelled as a single MTU. As a result, the actuation of a DoF can be simplified to only two MTUs. In addition to evaluating these methods in simple motions in free space, recent studies have explored the robustness of lumped MTUs to different arm loadings [24] and postures [25] for able-bodied subjects. Preliminary results on the offline prediction of kinematics during 3-DoF motion have also been presented in [26] for an able-bodied subject. While promising for prosthesis control applications, these methods do not compute and use information about the muscle and joint impedance available from MTUs models.

Our approach makes use of lumped muscle-tendon models. However, in a departure from existing work, we define an optimization framework for training such models to estimate the user motor intent in terms of joint kinematics, stiffness, and damping without using a reference joint torque or stiffness.

B. Impedance control of upper-limb prostheses

Given the association between cocontraction of agonist/antagonist muscles and joint impedance [1], a signal defining the level of coactivation of agonist and antagonist muscles is typically used in control schemes that attempt to adapt the stiffness of the prosthesis. The coactivation index, also defined as stiffness index, is computed as the weighted sum of the amplitude of processed sEMG signals of agonist and antagonist muscles [27]. Difficulties in discriminating changes in sEMG signals associated with changes in joint position or joint stiffness were avoided by using sEMG signals from different muscle groups (chest and upper-limb) [28]. In [29], a cocontraction index and a task-specific threshold on muscle coactivation were used to limit the sensitivity of velocity-based proportional control to variations in muscles coactivation and enable an amputee to simultaneously control the velocity and stiffness of one DoF by only using a pair of sEMG sensors. Moreover, it was shown that the amputee preferred variable stiffness control to a fixed-gain high-stiffness controller. Other methods used reference joint torques and kinematics to learn a model of joint stiffness and damping (polynomial function of sEMG signals) [30], [31]. While these models have been used to implement an admittance filter to estimate the DoF kinematics from joint torque [31], the estimated stiffness and damping were not employed to implement a variable impedance controller on the robot.

Methods that use MTUs, do not estimate the joint stiffness from the muscle-tendon model's state and contraction dynamics; typically, the joint stiffness is either computed as a weighted sum of the amplitude of sEMG signals from agonist-antagonist muscles, or as the weighted sum of the joint torque generated by each muscle-tendon unit [32]. In [32], the stiffness index was linearly mapped by calibration to the desired stiffness range (i.e., joint stiffness) according to the subject's requirements, the type of task, and the robotic system. Joint damping was set to vary proportionally to the joint stiffness. The control performance provided by the framework was evaluated with an able-bodied subject on a knee exoskeleton. In the context of upper-limb exoskeletons, a similar approach to stiffness estimation was described in [33]. In [34], the joint stiffness and position of a single DoF were estimated from a pair of sEMG signals using two hyperbolic tangent models driven by the sum and the difference of the amplitude of processed sEMG signals, respectively.

Finally, there has been a limited evaluation of the control performance provided by previous methods in relation to the modulation of stiffness [28], [30]–[32], [34].

C. Contributions of this work

We make the following contributions:

- We describe AIC-UP, an sEMG-based framework, that enables the user to voluntarily adapt the kinematics, stiffness and damping of one DoF of a simulated robot through wrist flexion-extension. AIC-UP comprises a "Detection of human motor intent" component (Figure 1-A) that incorporates lumped muscle-tendon models, and the "Prosthesis control" component to execute the estimated motor intent through a simulated robotic system based on a position-based variable impedance controller.
- The framework's design is constrained by the application domain. Unlike prior work (Section I-B), we assume the impossibility of measuring joint torque and stiffness trajectories to optimise the muscle-tendon models. This problem is tackled by enriching the dataset used to train muscle-tendon models, designing a novel optimization framework, and by imposing constraints on the parameter space of muscle-tendon models.

We evaluated AIC-UP with eight able-bodied subjects performing reaching tasks in free space and in the presence of unexpected external perturbations. A case study was also carried out with a transradial amputee. AIC-UP was compared with a baseline comprising a neural network trained to learn a mapping from sEMG to joint kinematics without explicitly learning and estimating the joint stiffness or damping.

II. METHODOLOGY

We first describe the two components of AIC-UP, highlighted in Figure 1-A in pink and blue. Then, Section II-C provides a solution to the ill-posed problem of estimating the value of the parameters of MTUs in the absence of a reference joint torque and stiffness. As an example of a controlled robotic system, we simulate the model of the *Puma 560* robot because its characteristics are well-understood; we consider the chain from link 0 to link 2 and control joint 2. The simulation is implemented using CoppeliaSim [35] and MATLAB [36]. For simplicity, the time dependence of variables is dropped in the description below.

A. Detection of human motor intent

The first component of AIC-UP maps the preprocessed sEMG signals of the agonist and antagonist muscles (ch_1, ch_2) to an estimate of the user's motion intent as joint kinematics, stiffness and damping (s_r, K, D) in two phases detailed below.

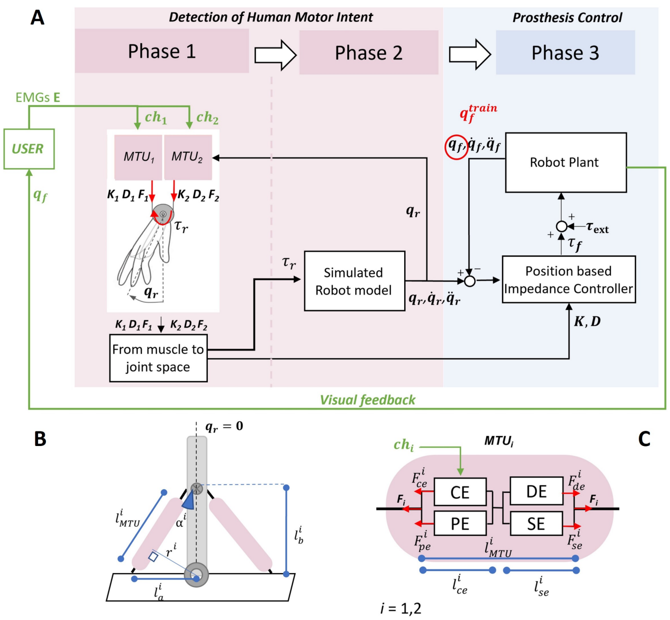

Fig. 1. (A) Overview of our framework AIC-UP. It comprises a *Detection of Human Motor Intent* block which includes muscle-tendon models and a *Prosthesis Control* block. The framework outputs the predicted joint position $\boldsymbol{q_f}$, the joint stiffness $\boldsymbol{K}$ and damping $\boldsymbol{D}$. The joint position $\boldsymbol{q_f}$ is used as an optimisation signal for training the muscle-tendon units parameters and it is the visual feedback provided to the subject during online control. (B) Arrangement of the $\boldsymbol{MTUs}$ on the link of the "simulated robot model". The "Robot plant" has the same structure and dynamics of the "simulated robot". (C) Forces generated by the $\boldsymbol{MTU}$'s muscle (CE, PE) and tendon components (DE, SEE) respectively.

1) Phase 1 - Muscle-tendon contraction dynamics: Two lumped MTUs were used to model the macroscopic properties of agonist and antagonist muscles, based on the Hill's muscle-tendon model [37]. Specifically, we adopted the model structure discussed in [38], where it was shown how the serial damping element (DE) enabled the suppression of high-frequency oscillations within the model. Each MTU_i of length l^i_{MTU} is composed of a muscle of length l^i_{ce} in series to a tendon of length l^i_{se}. The muscle is modeled by a contractile element (CE) and a parallel elastic element (PE). The tendon comprises an elastic element (SE) in parallel to DE, both added in series to the muscle (Figure 1-C). Given ch_i, CE generates a force F^i_{CE} as a function of l^i_{ce} and contraction velocity $\dot{l}^i_{ce}$. The contraction dynamics of both MTUs predicts the muscle-tendon forces (F_1, F_2). The state of the MTUs $(l_{ce}, \dot{l}_{ce})$ at the next time step is obtained at the end of phase 2 of the framework component, since it also depends on the predicted joint position q_r of the "Simulated robot model".

2) Phase 1 - Muscle-tendon stiffness and damping: Among the approaches detailed in Section I-B, in AIC-UP the stiffness K_i and damping D_i of each MTU_i is estimated from the MTU_i state and then mapped to the simulated robot's joint space. K_i is modeled as the muscle stiffness K^i_m in series with the tendon stiffness K^i_t, computed as $K_i = K^i_m K^i_t/(K^i_m + K^i_t)$. D_i is modelled as the muscle damping in series with the tendon damping and computed in the same way. We compute K^i_m as the directional derivative of F_m with respect to unit vector of l^i_{ce} [39]:

$$K^i_m = \frac{\partial F^i_m(l^i_{ce}, \dot{l}^i_{CE}, ch_i)}{\partial l^i_{ce}} \tag{1}$$

This formulation, differently from the stiffness index (Section I-B), takes into account the state of the muscle $(l^i_{ce}, \dot{l}^i_{ce}, ch_i)$ and it removes the contribution to stiffness due to changes in muscle force due to changes in $\dot{l}^i_{ce}$ and ch_i. Similarly, K^i_t is computed as the directional derivative of $F^i_t = F^i_{se} + F^i_{de}$ with respect to unit vector of $l^i_{se} = l^i_{MTC} - l^i_{ce}$. While muscle damping D^i_m was not computed in [39], we obtained it as directional derivatives of F^i_m with respect to $\dot{l}^i_{ce}$ unit vector as follows:

$$D^i_m = \frac{\partial F^i_m(l^i_{ce}, \dot{l}^i_{ce}, ch_i)}{\partial \dot{l}^i_{ce}} \tag{2}$$

The tendon damping D^i_t was computed as directional derivative of F^i_t with respect to the tendon extension velocity $\dot{l}^i_{se} = \dot{l}^i_{MTU} - \dot{l}^i_{ce}$ unit vector.

3) Phase 1 - Geometric arrangement of MTUs on robot's link: Figure 1-B shows the geometric arrangement of the MTUs on the simulated robot link. Each MTU_i is virtually attached to the link from the Center of Mass (CoM) (l^i_b) to a fixed base (l^i_a). The length l^i_{MTU} is dependent on q_r. Given the parameters α^i and the initial joint position $q_r = 0$, we can compute l^i_a as $l^i_{MTU} \sin \alpha^i$. The values of l^i_a and l^i_b are constant and identified based on the position of CoM and the initial length of the MTUs. The MTUs length $l^i_{MTU}(q_r)$ and moment arm $r^i(q_r)$ vary as function of q_r:

$$l^i_{MTU}(q_r) = \sqrt{(l^i_a)^2 + (l^i_b)^2 - 2 l^i_a l^i_b \cos(\pi/2 - q_r)} \tag{3}$$

Next, the muscle-tendon forces, stiffness, and damping are mapped to joint space quantities using the Jacobian matrix $\mathbf{R}(q_r) = [r^1(q_r)\ r^2(q_r)]^T = [\frac{\partial l^1_{MTU}(q_r)}{\partial q_r}\ \frac{\partial l^2_{MTU}(q_r)}{\partial q_r}]^T$ containing the moment arms r^i of the two MTUs:

$$\begin{aligned} r^i(q_r) &= \frac{\partial l^i_{MTU}(q_r)}{\partial q_r} = l^i_b \sin \alpha^i(q_r) \\ \text{with} \quad \alpha^i(q_r) &= \operatorname{acos}\Big(\frac{-(l^i_a)^2 + (l^i_b)^2 + (l^i_{MTU})^2}{2 l^i_{MTU} l^i_b}\Big) \end{aligned} \tag{4}$$

4) Phase 1 - Mapping from muscle space to joint space: The net torque generated by applying the MTUs forces F_1 and F_2 with moment arms $\mathbf{R}$ is computed as $\tau_r = [F_1, F_2]^T \mathbf{R}$. Considering the definition of τ_r and the dependency of $\mathbf{R}$ on q_r [40], we compute K as follows:

$$K = \frac{\partial \tau_r(q_r)}{\partial q_r} = \frac{\partial \mathbf{R}^T}{\partial q_r}[F_1, F_2]^T + \mathbf{R}^T diag([\frac{\partial F_1}{\partial q_r}, \frac{\partial F_2}{\partial q_r}])\mathbf{R} \tag{5}$$

Where the derivatives $\frac{\partial F_i}{\partial q_r}$ is the stiffness of MTU_i. The joint damping is computed as $D = \sum_{i=1}^{2}(D_i(r^i)^2)$.

5) Phase 2 - Forward dynamics: At this stage, the human motor intent is represented by the joint torque τ_r, joint stiffness K, and damping D. The torque τ_r is applied at the robot's joint using its forward dynamic model, to obtain the reference motion $s_r = (q_r, \dot{q}_r, \ddot{q}_r)$ needed to implement the position-based impedance controller discussed below.

B. Prosthesis control

A position-based variable impedance controller is used to track s_r with K and D. The dynamic model for a robot with one rotational joint is:

$$M\ddot{q}_r + g(q_r) = \tau_f + \tau_{ext} \tag{6}$$

where M is the link's joint space inertia, g is the gravity compensation torque, and τ_{ext} is the external perturbation on the robot joint. We build on the impedance control method used in the absence of force-torque readings [41] to define the control law as follows:

$$\tau_f = M\ddot{q}_r + K(q_r - q_f) + D(\dot{q}_r - \dot{q}_f) + g(q_r) \tag{7}$$

This definition uses the robot's link inertia since only low accelerations are reached during control. We design the MTUs' length and contraction velocity to be a function of s_r so that any external perturbation τ_{ext} only affects $s_f = (q_f, \dot{q}_f, \ddot{q}_f)$, while s_r and the MTUs remain unaffected and represent the user motor intent based on the input sEMG signal. This enables the implementation of the user's "corrective action" in the impedance controller. In the absence of external perturbations ($\tau_{ext} = 0$), q_r matches q_f. If τ_{ext} is non-zero, depending on K and D, q_f will start diverging from q_r. Therefore, q_f serves as visual feedback for the user, who can perform run-time adaptation of the simulated robot's state and gains (K, D) by modulating the muscles' coactivation to reduce the error between q_r and q_f and achieve the desired performance.

C. Muscle-tendon models training

While the MTUs structure is defined based on [38], suitable values for the parameters of each MTU_i have to be defined. Table IV lists the parameters $\overline{\boldsymbol{p}}^i \in \mathbb{R}^m$ of MTU_i to be optimized. Related work uses a reference joint torque or joint stiffness (Section I-B) to optimise the MTUs models. As explained in Section I, our chosen domain of application is upper-limb prosthesis, meaning that we do not have access to any reference joint torque or stiffness. Solutions to this issue are described in the following.

1) Structural assumptions on MTU: Muscle-tendon systems characterised by a tendon longer than the muscle enhance control and impedance modulation [42], [43]. The hypothesis on the functional properties enabled by this MTU's structure has been investigated in [44]. We thus define MTUs with a long tendon compared to the muscle, by setting the tendon slack length to $\frac{2}{3}l^i_{MTU}$. The muscle and tendon length ratio matches that of the muscle-tendon complex investigated in [44].

2) Simplification of MTU parameters: Model re-parametrization is detailed in Table IV. Sensitivity studies led to two model simplifications: (i) the pennation angle is set to be zero; (ii) The optimal length l^i_{opt} is modelled as a constant parameter to be estimated, and not as function of the input activation [45].

3) Optimization signal: We collected sEMG signals and the corresponding reference trajectory q_f^{train} to optimise the MTUs within AIC-UP. We used the final joint position q_f, which depends on the dynamics defined by the gains (K, D), as the optimisation signal and collected examples of sEMG signals and reference trajectory performed at different levels of muscle coactivation (Section III-C.1). This important change enabled us to train the MTUs such that the stiffness and damping estimated from the MTUs' state can be incorporated directly into the position-based variable impedance controller without further tuning. Including the impedance controller in the optimization framework avoids a mismatch between the dynamics of the MTUs and the robot's one. Exemplary experimental results in support of the argument are provided in Appendix I and shown in Figure 6. The prediction function $f : \mathbb{R}^{2m+2} \to \mathbb{R}$ acts on the input defined by $[ch_1(t), ch_2(t)] \in \mathbb{R}^2$ and the parameters of the MTUs $\overline{\mathbf{p}} = [\overline{\mathbf{p}}^1, \overline{\mathbf{p}}^2] \in \mathbb{R}^{2m}$ to produce the final joint position $q_f(t) \in \mathbb{R}$. Then, the constrained optimization problem is:

$$\begin{aligned} \min_{\overline{\mathbf{p}}} \quad & \sqrt{\frac{\sum_{t=1}^{T}(f([ch_1(t), ch_2(t)]; \overline{\mathbf{p}}) - q_f^{train}(t))^2}{T}} \\ \text{s.t.} \quad & \mathbf{lb} \leq \overline{\mathbf{p}} \leq \mathbf{ub} \end{aligned} \tag{8}$$

where $q_f^{train}(t) \in \mathbb{R}$ is the measured wrist flexion-extension angular position; $\mathbf{lb}, \mathbf{ub} \in \mathbb{R}^{2m}$ are the lower and upper bounds of $\overline{\mathbf{p}}$ in Table IV, and T is the trajectory length. The following constraints are added to the optimization problem to prevent numerical instability, aid in convergence, and impose assumptions discussed in the section above:

- $W^i_{des} + W^i_{asc} < l^i_{ceInit}$, where l^i_{ceInit} is l^i_{ce} when $q_r = 0$, such that CE operates in the muscle-length range. W_{des} and W_{asc} are the width of the descending and ascending branches of the isometric curve, as indicated in [38].
- if $l^i_{ce} < 0.001 l^i_{opt}$ or $l^i_{ce} > 0.95(l^i_{MTU} - l^i_{see0})$ set $\dot{l}^i_{ce} = 0$ such that $l^i_{MTU} = l^i_{ce} + l^i_{see0}$ and tendon cannot be compressed. l_{opt} is the length at which the maximum isometric force is reached, l_{see0} is the tendon slack length.
- $K > 0, D \geq 0$; required for control stability.
- tendon maximum extension (l^i_{se}) is $0.1 \cdot l^i_{see0}$ [42].

III. EXPERIMENTAL EVALUATION

The experimental setup and protocol are illustrated in Figure 2. First, the data (E, q_f^{train}) were collected as needed to train AIC-UP and BL. Then, the trained model was used for an online control experiment where the subject was given real-time control of the (simulated) robot plant and had to perform target-reaching tasks in the free space and in the presence of unexpected perturbations.

A. Participants

Eight able-bodied volunteers (five females, three males, age: 27.87 ± 3.64, right-handed) without neuromuscular disorders and prior experience in myocontrol, and a transradial amputee (female, age 65) took part in the study approved by the ethics committee of the University of Birmingham (ERN_19-1564) and Imperial College London (18IC4685). The amputee participant was not a prosthesis user.

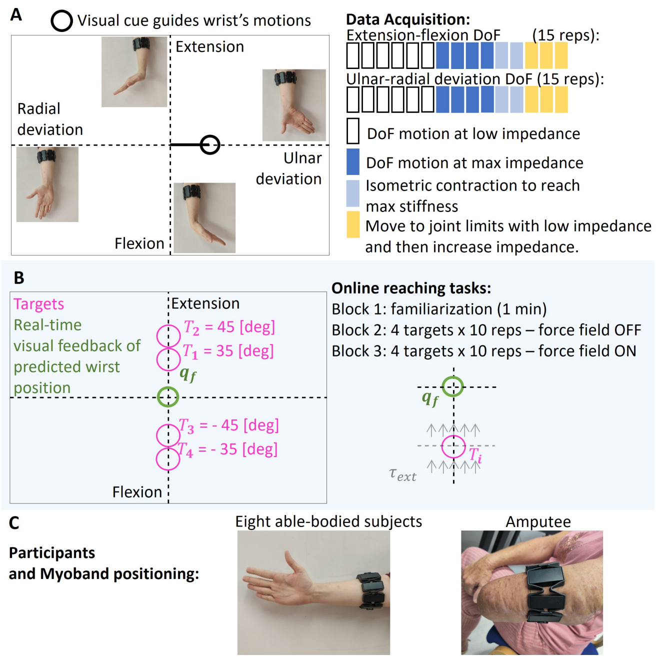

Fig. 2. **A)** Protocol for data collection $(\boldsymbol{E}, \boldsymbol{q}_f^{train})$ described in III-C.1. **B)** Online control experiment described in III-C.2. Note that the subject had no visual feedback on the force field, the force field in grey is represented here only for explanation. **C)** Position of EMG sensors on the subject's forearm. **D)** Questionnaire of perceived controllability.

B. Experimental setup

Each participant sat in front of a screen, with their arm in a neutral resting position along the body side. They wore a Myoband by ThalmicLab (eight sEMG channels, frequency 200 Hz) positioned $\approx$ 5 cm below the elbow (Figure 2-C). The raw sEMG signals were bandpass-filtered (20 - 500 Hz), and full-wave rectified; the root-mean-square temporal features were extracted with a moving window of length 160 ms and step size 40 ms. The sEMG signals recorded by the channels overlaying the Flexor Carpi Radialis and the Extensor Carpi Ulnaris were selected and normalized according to the maximum value recorded during the training phase to obtain the activation signals ch_1 and ch_2. The sEMG from all the channels of the Myoband were used for the baseline. The wrist position q_f^{train} was tracked with a Qualysis motion capture system for the able-bodied subject. For the amputee, q_f^{train} was the trajectory of the visual cue the participant had to follow during data acquisition experiment.

C. Experimental protocol

For each participant, experiments were conducted in three sessions. In the first session, we collected data to train AIC-UP and baseline (BL); the online control performance provided by AIC-UP and BL was then tested on two separate days to avoid muscle fatigue and involuntary bias due to the order in which frameworks were evaluated.

1) Data acquisition for muscle-tendon model training: During each trial, a visual cue moved along one of the axes and the subject had to move their wrist to proportionally match this cue. Each DoF motion was repeated 15 times while the subject was instructed to perform the wrist motion while modulating the muscle coactivation to achieve different levels of wrist impedance (Figure 2-A). We ensured that the subjects understood the concept of limb impedance by explaining to them that muscle cocontraction allows modulating limb rigidity, which affects the interaction with the external environment. Although we focus on the control of a single DoF (flexion-extension), we asked the subjects, during data collection only, to also perform repetitions of ulnar-radial deviation so that we could observe the "unintentional" flexion-extension motion and include these in the training dataset. The sEMG signals E and wrist position $\mathbf{q}_f^{train}$ from 15 trials of flexion-extension motion and the 15 indirect flexion-extension motions were collected. A 60-40 split of this data was used for training and validating the muscle-tendon models, with optimization based on Simulated Annealing [46] (500 iterations, 5000 function evaluations, initial value of temperature 300, annealing interval 50) since the cost function has discontinuous derivatives. The same overall process was followed for the amputee participant, except the trajectory of the visual cue (the black circle in Figure 2-A) was used as q_f^{train}.

2) Online testing. Target-reaching task: As shown in Figure 2-B, in each trial a participant had visual feedback of their predicted wrist position q_f (green circle) and was asked to perform wrist flexion-extension to accurately reach a target position T_i (purple circle). Once at the target, the subject had to maintain the position for three seconds. Every time the subject could not maintain the position for the set time the 3-second dwelling time was reset. The ratio between the radius of the circle for q_f and for the target T_i was $\frac{3}{4}$, requiring precise control. Experimental trials for each subject were divided into three blocks (Figure 2-B): familiarisation with the control interface; reaching tasks in the free space; and reaching tasks in the presence of a perturbation field τ_{ext} that pushed q_f away from the target. At the beginning of each session, the subject was told that different motor control strategies could be explored, (e.g., relaxed movement, changing muscle coactivation), but the subject had no prior knowledge of the method being tested. The subject was told that some force would perturb q_f, but no information about the force field (type, magnitude, location) was provided to avoid biasing their control strategy. This choice allowed us to investigate the user's (visual) perception of the external force field depending on the control method being used (Section III-D.2). A uniform force field was activated when the distance from the centers of the cursor q_f and the target was 15 [deg] (d in the equation of Figure 2) and pushed the cursor away from the target. The magnitude of the perturbation was defined as a percentage of the maximum torque $\tau_f^{max} = K^{max} q_r$ generated by the subject during training for AIC-UP by considering the maximum stiffness K^{max} across trials. The contribution of damping to τ_f^{max} was not considered due to its high dependence on joint velocity which could lead to values of τ_f^{max} unfeasible to counter during online control when the joint velocity is likely to be low due to the resistance opposed by the force field. The impact of different magnitudes of force field was investigated in preliminary studies, concluding that 10% of τ_f^{max} was adequate to provide visual feedback perceived by the subject as a perturbation of q_f to then trigger a change in control strategy, and to avoid muscle tiredness.

D. Data-driven baseline

The baseline used for comparison was a two-layer neural-network (NN) that learned a mapping from sEMG signals to q_f^{train} [6] and predicted q_r. The same training data were used for training AIC-UP and NN. The NN was trained to match the performance reported in [6]. To ensure accurate motion tracking and perturbation rejection, a high-stiffness ($K_B = 100[N/rad]$) proportional-derivative controller was added in cascade to the NN to track the predicted joint position q_r and obtain q_f. The damping was set assuming a critically damped system ($D_B = \sqrt{K_B/4}[Ns/rad]$) [47]. Notice that the definition of τ_f^{max} is suitable in relation to the proportional and derivative gains of the high-stiffness controller.

1) Performance measures: The design of target-reaching tasks to evaluate the online control of human-machine interfaces is common in the literature and it is based on Fitt's studies [48]. We selected six widely used performance measures [49] to quantify the task performance for four targets illustrated in Figure 2-B: (i) *Success Rate* (SR) [%]: proportion of successful trials, with a trial successful if the target is reached within 30 s and the target position held for 3 s; (ii) *Near Miss* (NM) [#]: number of times the subject entered the target circle, but did not maintain the position for 3 s; (iii) *Time to Reach* (TR) [s]: time to complete the trial, with 30 s as the maximum allowed time. All the measures are affected by distance to the target, which may impact the difficulty of the task and are thus weighted by an index of difficulty [49] considering the target circle radius and the distance form the origin to allow comparison across the four targets. To further characterise the impact of enabling joint stiffness and damping modulation for AIC-UP, to smooth out the oscillation imposed by the force field, we considered two additional performance measures: (iv) *Coactivation (CA)* was computed as $\bar{ch}_1 + \bar{ch}_2$, where $\bar{ch}_i$ is the normalised amplitude of the preprocessed EMG signal averaged across a trial. The same channels of the Myoband are used for AIC-UP and BL to obtain $\bar{ch}_i$. (v) *Smoothness (SPARC)* of q_f is computed using the SPARC measure [50]; we expected to observe a higher value of SPARC if the subject successfully countered the external perturbations and modulated the joint impedance to smooth out the oscillation faster. While BL has constant high stiffness and damping, AIC-UP required the user to modulate such values via muscle cocontraction; (iv) The *Mutual Information* (MI) between τ_f and q_r is used to quantify the predictability of q_r given τ_f; MI has been used in literature for dynamic system analysis (e.g., [51]). Since q_r is the unperturbed reference trajectory and τ_f is the torque that results in q_f, we expect MI to increase when q_r matches q_f, thus when the subject quickly counters the perturbation.

2) Survey of user's perception of controllability: We explored the user's *perceived controllability* provided by AIC-UP and BL, in terms of control intuitiveness, effectiveness and robustness asking the subjects to answer six questions about the control methods at the end of each experimental session (*Questionnaire* in Figure 2-D). We investigated if the subjects modulated joint impedance as a strategy to accomplish the task and asked them to describe the force field properties they understood while using the control methods and interacting with the perturbations. Users had to choose one of the following answers to the first three questions: good (A1), fair (A2), and poor (A3). We have resolved to use a 3-level Likert scale since we found that participants tended to avoid extreme-category responses or could not decide between categories 1-2 and 4-5, for a 5-levels scale. The remaining questions allowed free-form answers. The participants were unaware of the control method being evaluated when completing the questionnaire.

E. Independent stiffness control

To assess whether stiffness could be controlled independently from kinematics, we analysed the correlation between joint kinematics, muscle coactivation and joint stiffness and damping during the three phases of the reaching-target task performed in the presence of perturbations: phase 1) movement from the origin towards the target, before entering the force field; phase 2) moving in the force field, towards the target; phase 3) maintaining the target position for 3 seconds while countering the force field perturbations. We defined the following measures: i) $MI(q_r, K)$, the correlation between the joint position and joint stiffness computed as mutual information between the two variables; ii) $MI(\dot{q}_r, D)$, the mutual information between joint velocity and joint damping; iii) $MI(K, ch_1 + ch_2)$, mutual information between coactivation of muscles and joint stiffness; iv) the integral of joint stiffness $\int K$ and of vi) damping $\int D$.

IV. RESULTS

All participants completed the online reaching-task experiment with AIC-UP and BL, and the questionnaire. The Wilcoxon signed-rank test was used to measure the statistical significance (p-values < 0.05) between the distributions of performance measures for AIC-UP and BL. These were not normally distributed based to the Kolmogorov–Smirnov test.

A. Offline tracking results

In able-bodied subjects, the average root mean square error (RMSE) between the predicted and reference joint position obtained during offline testing was $RMSE_{AIC-UP} = 0.2291 \pm 0.0457$ [rad] and $RMSE_{BL} = 0.1763 \pm 0.0435$ [rad], for AIC-UP and BL respectively. BL achieved higher prediction accuracy than AIC-UP. For the amputee, the tracking errors were $RMSE_{AIC-UP} = 0.4014$ [rad] and $RMSE_{BL} = 0.5817$ [rad]. The substantially higher average RMS values for the amputee than the able-bodied subjects are mainly due to lack of reference wrist trajectory for the amputee.

B. Online control. Results for able-bodied subjects.

Figure 3-A shows the distribution of the average (across-trials) performance of the eight able-bodied participants. Statistically significant differences in distributions of average performance measures between AIC-UP and BL are indicated

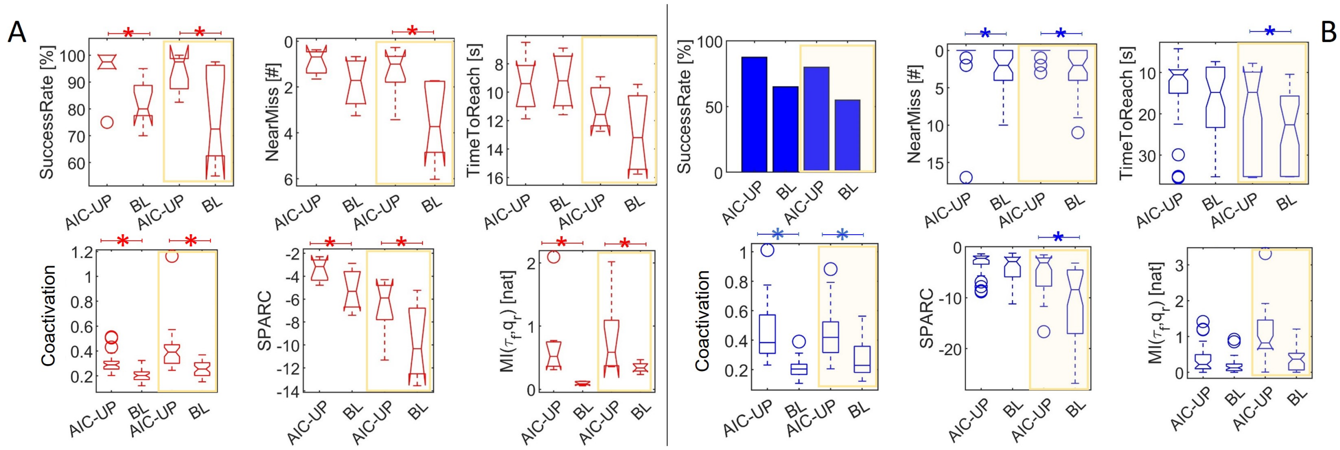

Fig. 3. Values of performance measures for the able-bodied subjects A) and the amputee B) in the absence and presence (highlighted in shaded yellow) of perturbations. A) Each group contains the average (across 40 trials) performance of the eight subjects; B) Each group contains the performance measure value of all trials. A statistically significant (p-value < 0.05) difference of the median are highlighted with an asterisk. Quantitative results describing the plots and the p-values are in Table I and Table II of Appendix II. Note that in B) the success rate is a single value for each group, no statistical analysis is considered.

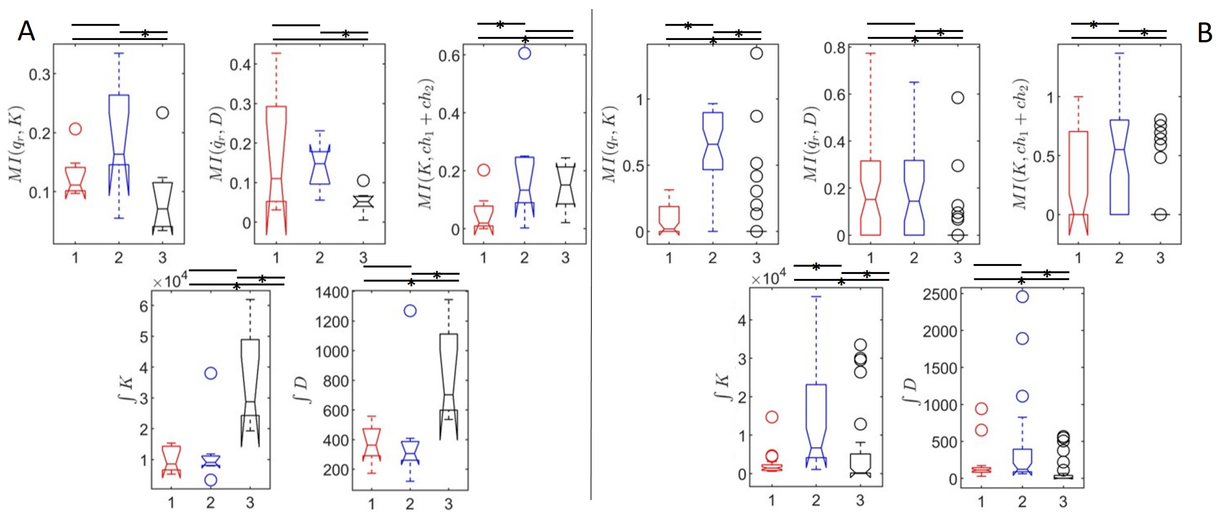

Fig. 4. Reaching-target tasks in the presence of perturbation are considered. For each measure, the distribution of average values across able-bodied participants (A), and across trials for the amputee (B), is computed in three distinct phases of the task, indicated in red, blue and black: (1) moving up to the force field, (2) crossing the force field to reach the target, (3) matching the target position for 3 seconds against perturbations. Statistically significant differences (p-value < 0.05) between median values of the task phases are indicated with an asterisk. Numerical values on statistically significant differences are in Table III of the appendix.

with a red asterisk at the top of the plot for the corresponding measure. In particular, the performance measures are compared for BL and AIC-UP when performing the task in the same condition (i.e., perturbation off, and on). The SR, NM and TR matrices are first considered to evaluate the task completion. Unlike BL, AIC-UP consistently enabled successful task completion with or without perturbation: the average SR metric was 95% and 82.19% for AIC-UP and BL (respectively) without perturbation, and 93.75% and 76.87% with perturbation. AIC-UP had a significantly lower number of NM during tasks in the presence of perturbations meaning that the subjects using AIC-UP were able to more precisely maintain the target position. The distributions of NM are in agreement with the task success rate. While the time to reach (TR) the target was not significantly lower for AIC-UP than BL, it can be observed that BL had a larger interquartile range, which is explained by the higher number of NM. The flexor-extensor coactivation was significantly higher when the subjects used AIC-UP instead of BL, indicating the active modulation of coactivation to achieve the task. While CA has a degree of correlation to joint stiffness, it is subject to variability due to the different strategies the subjects may adopt and depending on the control method being used. SPARC was greater with AIC-UP than with BL indicating that participants were able to smooth out the oscillations imposed by perturbations when using AIC-UP through modulation of the muscle coactivation. For BL, oscillations are bound to the accuracy of the estimates provided by the NN (see Figure S3 in the Supplementary Information). Finally, we observed that AIC-UP provided a significantly higher MI between τ_f and q_r compared with BL,

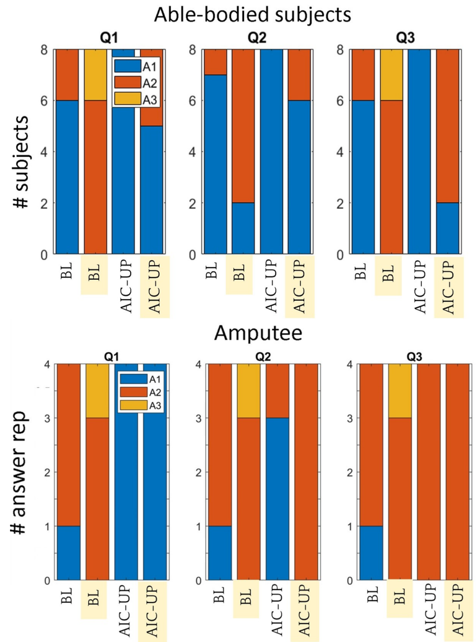

Fig. 5. Able-bodied participants and amputee's responses to Q1-3 of the questionnaire, completed at the end of the session with or without external perturbations (highlighted in yellow). For able-bodies, each category shows the fraction of subjects who provided a certain answer. For the amputee, the same question is asked every 10 trials, and the 4 answers are shown. The participants could choose among good (A1); fair (instances of low controllability) (A2); poor (A3).

with or without perturbation, suggesting that the participants using AIC-UP were able to modulate the joint stiffness and damping, used in the control law to obtain τ_f, to successfully complete the task and address the perturbations if needed. Overall, these results indicate that AIC-UP outperformed BL and effectively enabled joint stiffness and damping modulation through coactivation of agonist and antagonist muscles.

We investigated the perceived controllability of AIC-UP and BL among subjects; results for Q1-Q3 are summarized in Figure 5. Subjects indicated that AIC-UP provided a better match between motor intent and cursor motion, resulting in a more timely execution of motor commands, and more precise control than BL; these differences between the two controllers were more pronounced with perturbations. For Q4, six out of eight subjects gave a correct description of the perturbation field when using AIC-UP while two subjects were unsure; with BL, five out of eight subjects could not correctly describe the location of the force field and the others were unsure. For Q5, all the subjects had the same control strategy with BL: adopt low muscle cocontraction and move the wrist until the joint limit is reached. With AIC-UP, two subjects did not significantly increase muscle cocontraction, but the other six adapted joint impedance to counter perturbations. For Q6, all subjects agreed impedance modulation did not improve performance with BL; two subjects stated that it resulted in the worst perceived controllability. With AIC-UP, on the other hand, six out of eight subjects indicated that impedance adaptation helped counter perturbations; two subjects were unsure. These results support and correspond to the quantitative results in Figure 3-A.

C. Online control. Results for the amputee.

The values of performance measures obtained over the 40 trials per session by the amputee participant are reported in Figure 3-B. We observed that AIC-UP provided a higher SR than BL, with or without perturbation: average values were 87.50% and 65% for AIC-UP and BL without perturbations, and 80% and 55% with perturbations. NM was significantly higher with BL than with AIC-UP in the presence and absence of perturbations, which is in accordance to the relative SR. While there was no significant difference in TR for the able-bodied participants, for the amputee AIC-UP provided a significantly shorter TR than BL in the presence of perturbations. When the amputee used AIC-UP, there was a significant increase in coactivation. Moroever, SPARC and MI between τ_f and q_r were significantly greater with AIC-UP than with BL, with or without perturbation.

Finally, in Figure 5 the amputee's responses to Q1-Q3 are shown; we asked the subject to answer questions four times per session in an attempt to obtain more reliable answers. Similar to the responses from able-bodied participants, the amputee indicated that AIC-UP provided better controllability than BL, and correctly described the force field (Q4) with AIC-UP. For Q5, the amputee's control strategy when using BL changed from tensing up the muscles to trying to minimally co-activate the muscles "or the cursor would jump too far"; this was an example of the baseline incorrectly assigning an increase in activation to a change in position. When using AIC-UP, the amputee focused on cocontracting the muscles of the forearm when needed. For Q6, the subject was unsure if impedance modulation by muscle coactivation improved the performance with BL since the cursor would sometimes oscillate unexpectedly; with AIC-UP, however, she indicated three times that stiffening the muscles helped to counter the perturbations, and mentioned that it once led to some overshoot. Overall, these results support and match the quantitative results.

D. Modulation of joint kinematics and impedance

For able-bodied participants (Figure 4-A), there was a statistically significant decrease in correlation between joint position q_r and stiffness K between phase 2 and 3, and also between joint velocity and joint damping. In fact, in phase 3 the subject has to maintain the position while modulating K. Notably, the correlation between K and coactivation is significantly higher in phase 2 and phase 3 than in phase 1 where no perturbation is applied. Finally, the median value of $\int K$ in phase 3, was significantly higher than in the other phases. This is in agreement with experimental studies showing that static stiffness is higher than the stiffness reached during dynamic movements [52]. The same can be observed for $\int D$, higher in phase 3 than in phases 1 and 2; in phase 3 the muscle-tendon models operate mostly in isometric conditions and the muscle has low contraction velocities. Overall, these results indicate that the participants modulated the values of K and D by changing the muscles' coactivation in a time and task-dependent manner. The same can be observed for the amputee, with statistically significant differences between all three phases for also the measures MI(q_r, K), and $\int K$. The higher correlation between coactivation and stiffness in all phases than for able-bodies subjects can be explained by considering that the amputee's flexors and extensors operate in isometric conditions. However, $\int K$ and $\int D$ were higher in phase 2 than in phases 1 and 2 indicating that the amputee might have coactivated the muscles throughout phase 1 and phase 2. Consider that phase 2 and phase 3 have different durations, which impact $\int K$ and $\int D$.

V. DISCUSSION AND CONCLUSION

We described AIC-UP, a novel sEMG-based interface to voluntarily control the kinematics and the joint impedance (stiffness and damping) of a DoF of a simulated robot. Unlike prior work, two lumped muscle-tendon units were used to decode the motor intent in terms of joint kinematics, stiffness and damping. This required a reparametrization and structural assumption of the muscle-tendon units, and the design of an optimization framework to train the muscle-tendon models that included the impedance controller (Section II-C). In contrast to previous work, our framework does not require the measurement of joint torque or stiffness to train the models and it is therefore suitable for application in upper-limb prosthesis control. Note that we do not claim to learn stiffness and damping values that match the biological ones. Instead, our AIC-UP provides a coherent representation of the dynamics of the MTUs and that of the robot, leading to improved controllability. We showed that AIC-UP resulted in a significantly higher performance compared to the control BL, and allowed the able-bodied participants to exploit joint stiffness and damping adaptation as a means to modulate the physical interaction between the robot's plant and the environment. We further demonstrated that correlation between joint kinematics and stiffness or damping is substantially different during task execution, suggesting that AIC-UP enables time and task dependent modulation of stiffness and damping regardless of the joint position. While the methods were tested with a single amputee, the obtained results were coherent with those of the able-bodied participants.

In this work, we focused on a single DoF to isolate confounding factors. The insight we obtained will be used to expand AIC-UP to multi-DoF control. While lack of evaluation on a real prosthesis may be considered a limitation, we believe that the framework design and testing in a simulated environment, in the absence of physical constraints imposed by the hardware, is a necessary step towards improving methods for estimation of motor intent from sEMG signals. Observations from experimental results in simulation may be used as a performance baseline for when the framework is used to control a real robotic system. Moreover, because the chosen application domain is prosthesis control, we do not use a model of the biological limb, but we optimize the muscle-tendon models to implement the desired motor intent on a given robotic system; AIC-UP can be thus applied to any other robotic system with know kinematic and dynamic properties. In conclusion, our framework makes a step towards enabling impedance adaptation of prosthesis. While upper-limb prostheses was the chosen application domain, the approach may also be relevant in other rehabilitation device applications, or in human-robot-interaction scenarios, such as teleoperation.

APPENDIX OVERVIEW

In Appendix I we provide exemplary results in support of including the impedance controller in the optimization framework for estimating MTUs' parameters values. Appendix II provides numerical values and statistics to support the experimental results in Section III. In the Supplementary Information, we show the time evolution of values of MTUs' and joint variables during task trials.

APPENDIX I
IMPEDANCE CONTROLLER IN OPTIMIZATION FRAMEWORK

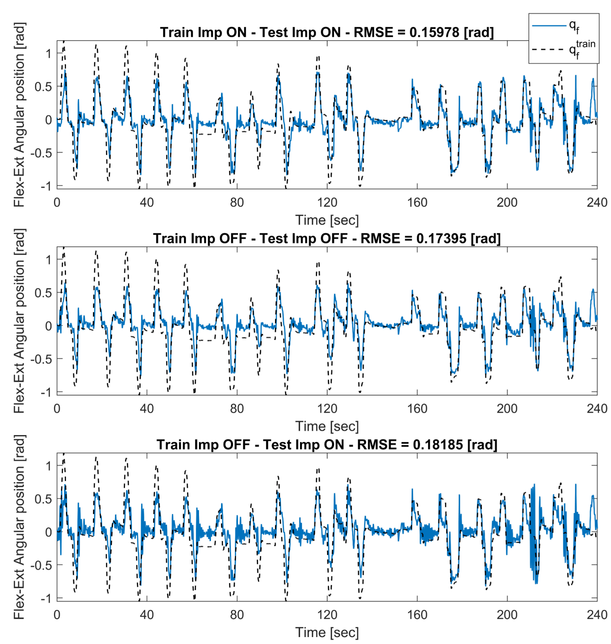

Fig. 6. Trajectory tracking during offline evaluation of AIC-UP. The black dotted line is the ground truth position. The blue line is the predicted trajectory under the following conditions: (top) framework optimization and evaluation included the impedance controller; (center) framework training and testing did not include the impedance controller; and (bottom) the optimization framework did not include the impedance controller, but the evaluation framework included the impedance controller.

As discussed in Section II-C, our optimization method uses q_f as an optimization signal, which is affected by the use of K and D as gains of the position-based impedance controller. Existing methods(Section I-B) instead use the joint torque τ_r and q_r as optimization signal. A reference joint stiffness may also be used. In this example, we trained the MTUs using q_r as optimization signal (60% of collected data), i.e., the impedance controller and the robot's plant were not included in this training process. We then evaluated the trained MTUs on the entire dataset (for completeness) as part of the entire framework that includes the impedance controller and the robot's plant (Figure 6, third plot). We showed that K and D cannot be used directly as gains in the impedance controller

TABLE I

DATA IN SUPPORT OF RESULTS FOR ABLE-BODIED PARTICIPANTS SHOWN IN FIGURE 3-A. WILCOXON SIGNED-RANK TEST IS USED TO ASSESS STATISTICALLY SIGNIFICANT DIFFERENCES (P-VALUE < 0.05) BETWEEN AIC-UP AND BL.

	Perturbations OFF					Perturbations ON				
	AIC-UP		BL			AIC-UP		BL		
	Median	IQR	Median	IQR	P-value ($<$ 0.05)	Median	IQR	Median	IQR	P-value ($<$ 0.05)
SR	97.50	5	80	11.25	0.009	97.50	11.25	72.50	33.75	0.03
NM	0.68	0.92	1.71	1.86	0.06	1.00	1.12	3.72	3.10	0.004
TR	9.39	2.89	9.19	3.48	0.87	11.57	2.68	13.19	5.18	0.13
CA	0.28	0.06	0.20	0.06	p <0.001	0.39	0.14	0.25	0.10	p <0.001
SPARC	-3.16	1.76	-5.32	3.08	0.04	-5.90	2.98	-10.32	5.72	0.06
MI	0.52	0.38	0.08	0.05	p <0.001	0.58	0.71	0.33	0.11	0.03

TABLE II

DATA IN SUPPORT OF RESULTS FOR THE AMPUTEE, SHOWN IN FIGURE 3-B. WILCOXON SIGNED-RANK TEST IS USED TO ASSESS STATISTICALLY SIGNIFICANT DIFFERENCES (P-VALUE $< \mathbf{0.05}$) BETWEEN AIC-UP AND BL.

	Perturbations OFF					Perturbations ON				
	AIC-UP		BL			AIC-UP		BL	BL	
	Median	IQR	Median	IQR	P-value (<0.05)	Median	IQR	Median	IQR	P-value (<0.05)
NM	0	0	2	4	$p < 0.001$	0	0	2	4	$p < 0.001$
TR	10.55	5.65	14.81	14.57	0.12	14.80	25.27	22.65	19.47	0.06
CA	0.44	0.30	0.22	0.07	$p < 0.001$	0.49	0.24	0.30	0.25	$p < 0.001$
SPARC	-2.26	1.60	-2.91	3.83	0.06	-3.15	5.54	-8.42	12.48	$p < 0.001$
MI	0.21	0.39	0.12	0.18	0.02	0.82	0.79	0.36	0.46	$p < 0.001$

TABLE III

DATA IN SUPPORT OF RESULTS IN FIGURE 4. WILCOXON SIGNED-RANK TEST IS USED TO ASSESS STATISTICALLY SIGNIFICANT DIFFERENCES (P-VALUE < 0.05) BETWEEN MEDIAN VALUES OF THE TASK PHASES FOR ABLE-BODIED SUBJECTS AND THE AMPUTEE WHEN USING AIC-UP.

	Able-bodied subjects			Amputee		
	AIC-UP (Perturbation ON)			AIC-UP (perturbation ON)		
	Phase 1 - 2	Phase 2 - 3	Phase 1 - 3	Phase 1 - 2	Phase 2 - 3	Phase 1 - 3
	P-value (<0.05)	P-value (<0.05)	P-value (<0.05)	P-value (<0.05)	P-value (<0.05)	P-value (<0.05)
$MI(q_r, K)$	0.12	0.02	0.09	$p < 0.001$	$p < 0.001$	0.01
$MI(\dot{q}_r, D)$	$p > 0.9$	0.006	0.16	0.89	$p < 0.001$	$p < 0.001$
$MI(K, ch_1 + ch_2)$	0.07	0.90	0.03	0.01	$p < 0.001$	0.06
$\int K$	0.90	0.01	0.001	0.01	$p < 0.001$	$p < 0.001$
$\int D$	0.53	0.01	0.001	0.17	$p < 0.001$	$p < 0.001$

and that this leads to oscillatory behavior and instabilities of the robot's plant. This explains why in related works the MTUs stiffnesses were tuned to implement a position-based control on the robot. This solution allows stable control but does not support the key requirement of matching the MTUs dynamics with the robot's dynamics. Figure 6 shows the offline evaluation of the framework when (i) the optimization and evaluation framework **included** the impedance controller; (ii) **did not include** the impedance controller; (iii) when the optimization framework **did not include** the impedance controller, but the evaluation framework did.

APPENDIX II
QUANTITATIVE VALUES AND STATISTICS

In Table I and Table II we report the median and interquartile range (IQR) values of the distributions of average performance measures shown in Figure 3-A and Figure 3-B, for AIC-UP and BL. Results obtained during trials performed in the absence and presence of perturbation are shown on the left and right sides of the tables. We test the significance (p-value < 0.05) of the difference in performance provided by AIC-UP and BL in the case of "perturbation off" and "perturbation on" using Wilcoxon signed-rank and reported the p-values in the tables. In Table III we report the p-values in support of the results in Figure 4. In Table IV we report the list of parameters optimised for each MTUs, the lower and upper bound of such values, as discussed in Section II-C.

ACKNOWLEDGMENT

The authors thank Deren Barsakcioglu, Irene Mendez Guerra, Milia Helena Hasbani, and Patrick G Sagastegui Alva for their support in conducting the experiments at ICL.

TABLE IV
PARAMETERS $\bar{\boldsymbol{p}}^{\boldsymbol{i}}$ OF $\boldsymbol{MTU^i}$ ESTIMATED DURING MODEL OPTIMIZATION; SEE [38] FOR DETAILS. THE COLUMN "VARIABLE" DETAILS OUR RE-PARAMETRIZATION. THE LOWER AND UPPER BOUNDS ARE SET EXPERIMENTALLY AND BASED ON PRIOR WORK [53].

Parameter Name	Variable	Lower Bound	Upper Bound
F_{max}	$\bar{p}_1$	1000	6000
v_{pee}	$\bar{p}_{10}$	1.1	3
l_{opt}	$\bar{p}_2 l_{ce}^{init}$	$0.05 l_{ce}^{init}$	$0.085 l_{ce}^{init}$
f_{pee0}	$\bar{p}_1 \bar{p}_{11}$	$0.5\bar{p}_1$	$1\bar{p}_1$
W_{des}	$\bar{p}_2 \bar{p}_3$	$0.7\bar{p}_2$	$3.5\bar{p}_2$
D	$\bar{p}_{12}$	0.001	3
W_{asc}	$\bar{p}_2 \bar{p}_4$	$0.7\bar{p}_2$	$3.5\bar{p}_2$
R	$\bar{p}_{13}$	0	0.8
v_{des}	$\bar{p}_5$	1.2	3
l_{see0}	$\frac{2}{3} l_{MTU}$	$\frac{2}{3} l_{MTU}$	$\frac{2}{3} l_{MTU}$
v_{asc}	$\bar{p}_6$	1.2	3
ΔUnl	$\bar{p}_{14}$	0.02	0.07
A_{max}	$\bar{p}_7$	0.1	0.4
ΔUl	$\bar{p}_{14} \bar{p}_{15}$	$\frac{1}{3}\bar{p}_{15}$	$\frac{2}{3}\bar{p}_{15}$
B_{max}	$\bar{p}_8$	1.1	5.1
ΔF_{see0}	$\bar{p}_1 \bar{p}_{16}$	$0.3\bar{p}_1$	$1\bar{p}_1$
l_{pee0}	$\bar{p}_2 \bar{p}_9$	$0.7\bar{p}_2$	$0.95\bar{p}_2$
S	$\bar{p}_{17}$	1.2	2
F	$\bar{p}_{18}$	0.5	2

REFERENCES

[1] Neville Hogan. Adaptive control of mechanical impedance by coactivation of antagonist muscles. *IEEE Transactions on automatic control*, 29(8):681–690, 1984.

[2] Mathilde Connan, Eduardo Ruiz Ramírez, Bernhard Vodermayer, and Claudio Castellini. Assessment of a wearable force-and electromyography device and comparison of the related signals for myocontrol. *Frontiers in neurorobotics*, 10:17, 2016.

[3] Ning Jiang, Johnny LG Vest-Nielsen, Silvia Muceli, and Dario Farina. Emg-based simultaneous and proportional estimation of wrist/hand kinematics in uni-lateral trans-radial amputees. *Journal of neuroengineering and rehabilitation*, 9(1):42, 2012.

[4] Janne M Hahne, F Biessmann, Ning Jiang, H Rehbaum, Dario Farina, FC Meinecke, K-R Müller, and LC Parra. Linear and nonlinear regression techniques for simultaneous and proportional myoelectric control. *IEEE Transactions on Neural Systems and Rehabilitation Engineering*, 22(2):269–279, 2014.

[5] Lauren H Smith, Todd A Kuiken, and Levi J Hargrove. Evaluation of linear regression simultaneous myoelectric control using intramuscular emg. *IEEE Transactions on Biomedical Engineering*, 63(4):737–746, 2015.

[6] Ning Jiang, Ivan Vujaklija, Hubertus Rehbaum, Bernhard Graimann, and Dario Farina. Is accurate mapping of emg signals on kinematics needed for precise online myoelectric control? *IEEE Transactions on Neural Systems and Rehabilitation Engineering*, 22(3):549–558, 2013.

[7] Ning Jiang, Hubertus Rehbaum, Ivan Vujaklija, Bernhard Graimann, and Dario Farina. Intuitive, online, simultaneous, and proportional myoelectric control over two degrees-of-freedom in upper limb amputees. *IEEE transactions on neural systems and rehabilitation engineering*, 22(3):501–510, 2013.

[8] D. Farina, N. Jiang, H. Rehbaum, A. Holobar, B. Graimann, H. Dietl, and O. C. Aszmann. The extraction of neural information from the surface emg for the control of upper-limb prostheses: Emerging avenues and challenges. *IEEE Transactions on Neural Systems and Rehabilitation Engineering*, 22(4):797–809, 2014.

[9] Johnny LG Nielsen, Steffen Holmgaard, Ning Jiang, Kevin B Englehart, Dario Farina, and Phil A Parker. Simultaneous and proportional force estimation for multifunction myoelectric prostheses using mirrored bilateral training. *IEEE Transactions on Biomedical Engineering*, 58(3):681–688, 2010.

[10] Silvia Muceli and Dario Farina. Simultaneous and proportional estimation of hand kinematics from EMG during mirrored movements at multiple degrees-of-freedom. *IEEE Transactions on Neural Systems and Rehabilitation Engineering*, 20(3):371–378, 2012.

[11] Nan Bu, Osamu Fukuda, and Toshio Tsuji. Emg-based motion discrimination using a novel recurrent neural network. *Journal of Intelligent Information Systems*, 21(2):113–126, Sep 2003.

[12] Peng Xia, Jie Hu, and Yinghong Peng. Emg-based estimation of limb movement using deep learning with recurrent convolutional neural networks. *Artificial organs*, 42(5):E67–E77, 2018.

[13] Tom Chau. A review of analytical techniques for gait data. part 2: neural network and wavelet methods. *Gait & posture*, 13(2):102–120, 2001.

[14] Ali Ameri, Mohammad Ali Akhaee, Erik Scheme, and Kevin Englehart. Regression convolutional neural network for improved simultaneous emg control. *Journal of neural engineering*, 16(3):036015, 2019.

[15] E. K. Chadwick *, D. Blana, A. J. van den Bogert, and R. F. Kirsch. A real-time, 3-d musculoskeletal model for dynamic simulation of arm movements. *IEEE Transactions on Biomedical Engineering*, 56(4):941–948, April 2009.

[16] DG Lloyd and TS Buchanan. A model of load sharing between muscles and soft tissues at the human knee during static tasks. *Journal of biomechanical engineering*, 118(3):367–376, 1996.

[17] Kurt Manal, Roger V Gonzalez, David G Lloyd, and Thomas S Buchanan. A real-time emg-driven virtual arm. *Computers in biology and medicine*, 32(1):25–36, 2002.

[18] Andrea Cimolato, Giovanni Milandri, Leonardo S Mattos, Elena De Momi, Matteo Laffranchi, and Lorenzo De Michieli. Hybrid machine learning-neuromusculoskeletal modeling for control of lower limb prosthetics. In *2020 8th IEEE RAS/EMBS International Conference for Biomedical Robotics and Biomechatronics (BioRob)*, pages 557–563. IEEE, 2020.

[19] Massimo Sartori, Monica Reggiani, Antonie J van den Bogert, and David G Lloyd. Estimation of musculotendon kinematics in large musculoskeletal models using multidimensional b-splines. *Journal of biomechanics*, 45(3):595–601, 2012.

[20] Thomas S Buchanan, David G Lloyd, Kurt Manal, Thor F Besier, et al. Estimation of muscle forces and joint moments using a forward-inverse dynamics model. *Medicine and Science in Sports and exercise*, 37(11):1911, 2005.

[21] Samuel K Au, Paolo Bonato, and Hugh Herr. An emg-position controlled system for an active ankle-foot prosthesis: an initial experimental study. In *9th International Conference on Rehabilitation Robotics, 2005. ICORR 2005.*, pages 375–379. IEEE, 2005.

[22] Dustin L Crouch and He Huang. Musculoskeletal model predicts multi-joint wrist and hand movement from limited emg control signals. In *2015 37th Annual International Conference of the IEEE Engineering in Medicine and Biology Society (EMBC)*, pages 1132–1135. IEEE, 2015.

[23] Dustin L Crouch and He Huang. Lumped-parameter electromyogram-driven musculoskeletal hand model: A potential platform for real-time prosthesis control. *Journal of biomechanics*, 49(16):3901–3907, 2016.

[24] Lizhi Pan, Andrew Harmody, and He Huang. A reliable multi-user emg interface based on a generic-musculoskeletal model against loading weight changes. In *2018 40th Annual International Conference of the IEEE Engineering in Medicine and Biology Society (EMBC)*, pages 2104–2107. IEEE, 2018.

[25] Lizhi Pan, Dustin L Crouch, and He Huang. Myoelectric control based on a generic musculoskeletal model: Toward a multi-user neural-machine interface. *IEEE Transactions on Neural Systems and Rehabilitation Engineering*, 26(7):1435–1442, 2018.

[26] Lizhi Pan, Dustin Crouch, and He Huang. Musculoskeletal model for simultaneous and proportional control of 3-dof hand and wrist movements from emg signals. In *2017 8th International IEEE/EMBS Conference on Neural Engineering (NER)*, pages 325–328. IEEE, 2017.

[27] Rieko Osu, David W Franklin, Hiroko Kato, Hiroaki Gomi, Kazuhisa Domen, Toshinori Yoshioka, and Mitsuo Kawato. Short-and long-term changes in joint co-contraction associated with motor learning as revealed from surface emg. *Journal of neurophysiology*, 88(2):991–1004, 2002.

[28] Elif Hocaoglu and Volkan Patoglu. sEMG-based natural control interface for a variable stiffness transradial hand prosthesis. *Frontiers in Neurorobotics*, 16, 2022.

[29] Patricia Capsi-Morales, Cristina Piazza, Manuel G Catalano, Antonio Bicchi, and Giorgio Grioli. Exploring stiffness modulation in prosthetic hands and its perceived function in manipulation and social interaction. *Frontiers in Neurorobotics*, page 33, 2020.

[30] Akira Furui, Shintaro Eto, Kosuke Nakagaki, Kyohei Shimada, Go Nakamura, Akito Masuda, Takaaki Chin, and Toshio Tsuji. A myoelectric prosthetic hand with muscle synergy–based motion determination and impedance model–based biomimetic control. *Science Robotics*, 4(31):eaaw6339, 2019.

[31] Toshio Tsuji, Keisuke Shima, Nan Bu, and Osamu Fukuda. Biomimetic impedance control of an em-based robotic hand. *Robot Manipulators: Trends and Development*, page 213, 2010.

[32] Nikos Karavas, Arash Ajoudani, Nikos Tsagarakis, Jody Saglia, Antonio Bicchi, and Darwin Caldwell. Tele-impedance based assistive control for a compliant knee exoskeleton. *Robotics and Autonomous Systems*, 73:78–90, 2015.

[33] Zhijun Li, Zhicong Huang, Wei He, and Chun-Yi Su. Adaptive impedance control for an upper limb robotic exoskeleton using biological signals. *IEEE Transactions on Industrial Electronics*, 64(2):1664–1674, 2016.

[34] Arash Ajoudani, Sasha B Godfrey, M Catalano, Giorgio Grioli, Nikos G Tsagarakis, and Antonio Bicchi. Teleimpedance control of a synergy-driven anthropomorphic hand. In *2013 IEEE/RSJ International Conference on Intelligent Robots and Systems*, pages 1985–1991. IEEE, 2013.

[35] E. Rohmer, S. P. N. Singh, and M. Freese. V-rep: A versatile and scalable robot simulation framework. In *2013 IEEE/RSJ International Conference on Intelligent Robots and Systems*, pages 1321–1326, 2013.

[36] The Mathworks, Inc., Natick, Massachusetts. *MATLAB version 9.5.0.1586782 (R2018b) Update 8*, 2018.

[37] Archibald Vivian Hill. The heat of shortening and the dynamic constants of muscle. *Proceedings of the Royal Society of London. Series B-Biological Sciences*, 126(843):136–195, 1938.

[38] Michael Günther, Syn Schmitt, and Veit Wank. High-frequency oscillations as a consequence of neglected serial damping in hill-type muscle models. *Biological cybernetics*, 97(1):63–79, 2007.

[39] Massimo Sartori, Monica Reggiani, Dario Farina, and David G Lloyd. Emg-driven forward-dynamic estimation of muscle force and joint moment about multiple degrees of freedom in the human lower extremity. *PloS one*, 7(12):e52618, 2012.

[40] Neville Hogan. Mechanical impedance of single-and multi-articular systems. In *Multiple muscle systems*, pages 149–164. Springer, 1990.

[41] Neville Hogan. Impedance control: An approach to manipulation: Part ii—implementation. 1985.

[42] Jack M Winters. Hill-based muscle models: a systems engineering perspective. In *Multiple muscle systems*, pages 69–93. Springer, 1990.

[43] MB Bennett, RF Ker, Nicola J Imery, and R McN Alexander. Mechanical properties of various mammalian tendons. *Journal of Zoology*, 209(4):537–548, 1986.

[44] PM Rack and HF Ross. The tendon of flexor pollicis longus: its effects on the muscular control of force and position at the human thumb. *The Journal of physiology*, 351(1):99–110, 1984.

[45] David G Lloyd and Thor F Besier. An emg-driven musculoskeletal model to estimate muscle forces and knee joint moments in vivo. *Journal of biomechanics*, 36(6):765–776, 2003.

[46] Peter JM Van Laarhoven and Emile HL Aarts. Simulated annealing. In *Simulated annealing: Theory and applications*, pages 7–15. Springer, 1987.

[47] Klas Kronander and Aude Billard. Learning compliant manipulation through kinesthetic and tactile human-robot interaction. *IEEE transactions on haptics*, 7(3):367–380, 2013.

[48] Paul M Fitts. The information capacity of the human motor system in controlling the amplitude of movement. *Journal of experimental psychology*, 47(6):381, 1954.

[49] Matthew R Williams and Robert F Kirsch. Evaluation of head orientation and neck muscle emg signals as command inputs to a human–computer interface for individuals with high tetraplegia. *IEEE Transactions on Neural Systems and Rehabilitation Engineering*, 16(5):485–496, 2008.

[50] Sivakumar Balasubramanian, Alejandro Melendez-Calderon, Agnes Roby-Brami, and Etienne Burdet. On the analysis of movement smoothness. *Journal of neuroengineering and rehabilitation*, 12(1):1–11, 2015.

[51] Salah Bazzi and Dagmar Sternad. Human control of complex objects: towards more dexterous robots. *Advanced Robotics*, 34(17):1137–1155, 2020.

[52] Andrew F Huxley and Ro M Simmons. Proposed mechanism of force generation in striated muscle. *Nature*, 233(5321):533–538, 1971.

[53] Carol Y Scovil and Janet L Ronsky. Sensitivity of a hill-based muscle model to perturbations in model parameters. *Journal of biomechanics*, 39(11):2055–2063, 2006.